Morphology of ion irradiation induced nano-porous structures in Ge and $Si_{1-x}Ge_x$ alloys

H. S. Alkhaldi, F. Kremer, P. Mota-Santiago, A. Nadzri, D. Schauries, N. Kirby, M. C. Ridgway, and P. Kluth

Citation: Journal of Applied Physics **121**, 115705 (2017); doi: 10.1063/1.4978592
View online: http://dx.doi.org/10.1063/1.4978592
View Table of Contents: http://aip.scitation.org/toc/jap/121/11
Published by the American Institute of Physics

Articles you may be interested in

Evidence for the formation of SiGe nanoparticles in Ge-implanted Si_3N_4
Journal of Applied Physics **121**, 105702 (2017); 10.1063/1.4977507

Carrier scattering in high-κ/metal gate stacks
Journal of Applied Physics **121**, 114503 (2017); 10.1063/1.4978357

Vortex-antivortex pairs induced by curvature in toroidal nanomagnets
Journal of Applied Physics **121**, 113906 (2017); 10.1063/1.4977983

Magnetic and microstructural properties of sputter deposited Cr-doped aluminum nitride thin films on silicon substrates
Journal of Applied Physics **121**, 115302 (2017); 10.1063/1.4978748

Suppression of gate leakage current in in-situ grown AlN/InAlN/AlN/GaN heterostructures based on the control of internal polarization fields
Journal of Applied Physics **121**, 115704 (2017); 10.1063/1.4978424

Physics-based analytical model for ferromagnetic single electron transistor
Journal of Applied Physics **121**, 113905 (2017); 10.1063/1.4978425

JOURNAL OF APPLIED PHYSICS 121, 115705 (2017)

Morphology of ion irradiation induced nano-porous structures in Ge and $Si_{1-x}Ge_x$ alloys

H. S. Alkhaldi,[1,2] F. Kremer,[3] P. Mota-Santiago,[1] A. Nadzri,[1] D. Schauries,[1] N. Kirby,[4] M. C. Ridgway,[1,a)] and P. Kluth[1]

[1]*Department of Electronic Materials Engineering, Research School of Physics and Engineering, The Australian National University, Canberra, ACT 2601, Australia*
[2]*Department of Physics, College of Education- Jubail, Imam Abdulrahman Bin Faisal University, Dammam 1982, Saudi Arabia*
[3]*Centre for Advanced Microscopy, Australian National University, Canberra, ACT 2601, Australia*
[4]*Australian Synchrotron, 800 Blackburn Road, Clayton, VIC 3168, Australia*

(Received 12 December 2016; accepted 1 March 2017; published online 21 March 2017)

Crystalline Ge and $Si_{1-x}Ge_x$ alloys ($x = 0.83$, 0.77) of (100) orientation were implanted with 140 keV Ge^- ions at fluences between 5×10^{15} to 3×10^{17} ions/cm^2, and at temperatures between 23 °C and 200 °C. The energy deposition of the ions leads to the formation of porous structures consisting of columnar pores separated by narrow sidewalls. Their sizes were characterized with transmission electron microscopy, scanning electron microscopy, and small angle x-ray scattering. We show that the pore radius does not depend significantly on the ion fluence above 5×10^{15} ions/cm^2, i.e., when the pores have already developed, yet the pore depth increases from 31 to 516 nm with increasing fluence. The sidewall thickness increases slightly with increasing Si content, while both the pore radius and the sidewall thickness increase at elevated implantation temperatures. *Published by AIP Publishing.*
[http://dx.doi.org/10.1063/1.4978592]

I. INTRODUCTION

Nanoporous semiconductors (Ge and Si) are technologically significant materials with various applications, e.g., in optoelectronic devices,[1] gas sensors,[2] drug delivery,[3] and energy storage.[4] Recently, there has been increasing interest in nanoporous Ge due to its higher carrier mobility and smaller band gap compared to nanoporous Si.[5] Nanoporosity also can be obtained in several compound semiconductors such as GaSb,[6] InSb,[7] and $Si_{1-x}Ge_x$.[8] The latter alloys are technologically important because the heterostructure can improve the properties of microelectronic devices such as heterojunction bipolar and complementary metal–oxide–semiconductor (CMOS) transistors.[1] In this work, ion implantation has been utilized to produce porosity in Ge and its alloys with Si. When ions with keV energies penetrate solids, they lose their energy predominantly through elastic interactions with the target nuclei. The resulting nuclear energy deposition into crystalline Ge can lead to a strong change in the surface morphology, including the formation of amorphous/nonporous layers. This phenomenon was observed using a variety of heavy ions and energies.[9–11] The threshold fluence for the formation of porosity in Ge ($\sim 10^{15}$ ions/cm^2 for several heavy ions) is about one order of magnitude larger than the amorphization threshold.[12] Compared to other methods, such as electrochemical etching, chemical/physical vapour deposition,[13] and spark processing,[14] ion implantation provides an inherently clean method of producing amorphous and porous layers, and it can create self-organized surface nanostructures (nanoporous structures), where pore sizes and depths can be controlled by tuning the implantation parameters.[12]

Controlling the pore size enables the design of materials with tailored properties including pore size, shape, and space in between pores. Specific applications, such as a zeolite (molecular sieves), require a uniform pore size distribution,[15] since the pore size distribution limits the ability of the solid to separate molecules of different sizes.[16] Thus, controlling the pore size is crucial to fabricate devices such as filters and catalysts.[1,17] However, there are other applications that require inhomogeneous pore size distributions such as visible light emission devices.[18] Therefore, it is necessary to determine the size distribution of the nanostructures, including the mean pore diameter and sidewall thickness. In order to correlate the morphology and the physical properties, precise statistical information of the pore size distribution and sidewall thickness of the surrounding material is required. The two main analytical methods that have been utilized in this study are Transmission Electron Microscopy (TEM) and Small Angle X-ray Scattering (SAXS).

TEM provides information about the size, structure, and arrangement of individual pores, which is restricted to a few hundreds of pores, and requires elaborate "destructive" sample preparation methods. Alternatively, SAXS can provide information about the particle size distribution, including various features of the nanostructures (e.g., pore radius, sidewall thickness) that are obtained for much larger areas including hundreds of millions of pores, and is considered a fast and non-destructive tool compared to TEM.[18–23] SAXS has been successfully applied to characterize porous structures in different materials systems. For instance, Engel *et al.*[24] utilized SAXS to analyse the pore size in polymer materials such as polycarbonate and in metal oxide such as alumina, where the pore arrangement ranged from random distributions up to highly ordered pores. SAXS has previously been used to investigate porous structures in Si, which

[a)]Deceased on 9 December 2015.

was mainly prepared by electrochemical etching.[18,22,25] Binder *et al.*[26] explained the scattering profile in terms of a bimodal distribution consisting of spherical and cylindrical pores oriented perpendicular to the surface. Mazumder *et al.*[22] showed oscillations in the scattering pattern corresponded to porous structure in Si. They estimated separate distributions for pore radius and pore length, but it is not clear whether these distributions were based on simulation or experimentally observed data.

In our previous study,[8] we quantified the nanostructure morphologies in Ge and $Si_{1-x}Ge_x$ alloys as a function of ion fluence at room temperature mainly by using SEM for measuring the pore size and TEM to provide information on porous layer thickness. In this study, we use SAXS combined with TEM to measure the pore size and sidewall thickness with regard to the entire bulk at both room temperature and elevated temperatures. We report an effect of ion fluence, implantation temperature, and Ge content on the structure size in nano-porous Ge and $Si_{1-x}Ge_x$ alloys prepared by ion implantation. We demonstrate that SAXS is an effective tool which provides new information on the nanoporosity which is in excellent agreement with TEM.

II. EXPERIMENTAL METHODS

The formation of porosity in this study was investigated for undoped crystalline Ge (c-Ge) and crystalline $Si_{1-x}Ge_x$ (c-$Si_{1-x}Ge_x$) alloys (x = 0.83, 0.77) of (100) orientation. The latter were prepared by molecular beam epitaxy (MBE) with a thickness of 2.5 μm grown on a Si substrate. To minimise parasitic scattering from the substrate during the SAXS measurements, the substrate was mechanically thinned down to ~170 μm. Ion implantation was performed at the ANU ion implantation facilities with 140 keV Ge^- at ion fluences ranging from 5×10^{15} to 3×10^{17} ions/cm^2. To study the effect of the implantation temperature, we have selected a fluence of 1×10^{16} ions/cm^2 for Ge and 1×10^{17} ions/cm^2 for $Si_{0.17}Ge_{0.83}$ and irradiated samples at temperatures ranging from RT to 200 °C.

As estimated by SRIM,[27] the nuclear energy loss at the surface $(dE/dx)_{nucl} = 1.4$ keV/nm is much higher than the electronic energy loss at the surface $(dE/dx)_{el} = 0.2$ keV/nm for Ge and its alloys, and thus, the latter is considered negligible. The projected ion ranges R_p for Ge, $Si_{0.17}Ge_{0.83}$, and $Si_{0.23}Ge_{0.77}$ are listed in Table I.

Cross-section transmission electron microscopy (XTEM) imaging was performed using a Philips CM300 microscope operating at 300 keV at The Centre of Advanced Microscopy at ANU. The TEM samples were prepared by using the conventional methods: mechanical grinding to 100 μm, dimple grinding to 10–20 μm and Ar ion milling.[28] The sample surface was imaged by plain-view scanning electron microscopy (PVSEM) using a Zeiss-UltraPlus FESEM.

The SAXS measurements were performed in transmission mode at the SAXS/WAXS beamline at the Australian Synchrotron, using an x-ray energy of 11 keV. A Pilatus 1M detector was used to record the scattering patterns with exposure times of 2, 5, and 10 s. The distance between the detector and the samples was set to 0.9 m. For alignment of the nano-porous structures, the samples were mounted on a three-axis goniometer, allowing precise tilting of the porous structures by 45° with respect to the incident x-ray beam. This orientation was preferred due to the non-spherical pore shape. For background removal, scattering from un-irradiated samples was measured.

III. RESULTS AND DISCUSSION

A. SAXS analysis

Fig. 1 shows schematics of the SAXS measurements, sample alignment, and detector images. The SAXS image in Fig. 1(a) shows isotropic scattering when the porous features of the sample are aligned parallel to the x-ray beam. The scattering pattern becomes anisotropic as shown in Fig. 1(b), when the sample is tilted by 45°. It resembles horizontally elongated scattering features that extend into short streaks or "bulges" reflecting the high aspect ratio of the aligned porous structures. The strong x-ray scattering contrast results from

TABLE I. SRIM simulation of projected ion Range R_p for 140 keV Ge^+ implanted into Ge, $Si_{0.17}Ge_{0.83}$, $Si_{0.23}Ge_{0.77}$, and $Si_{0.35}Ge_{0.65}$. The table also summarizes the core radii and shell thicknesses characterized by TEM and SAXS at room temperature for different ion fluences.

			Core radius R_c (nm)	Pore radius R_c (nm)	Shell thickness T_s (nm)	Sidewall thickness T_s (nm)	
Ge content	R_p (nm)	Ion fluence (ions/cm^2)	SAXS	TEM	SAXS	TEM	Polydispersity (nm)
1	62.2	5×10^{15}	11.8 ± 0.2	11.2 ± 2.5	13.5 ± 0.2	12.7 ± 1	2.7 ± 0.1
		1×10^{16}	23.9 ± 0.4	19.8 ± 4.2	9.8 ± 0.1	8.3 ± 2.2	2.9 ± 0.2
		2×10^{16}	21.5 ± 0.2	21 ± 4.7	8.4 ± 0.1	9.6 ± 1.9	5.6 ± 1.4
		5×10^{16}	18.9 ± 0.1	20 ± 4	9 ± 0.3	9.3 ± 1.8	2.7 ± 0.3
		1×10^{17}	14.6 ± 0.4	15 ± 4	10.6 ± 0.1	9.3 ± 1.6	4 ± 0.2
		2×10^{17}	22.2 ± 0.2	…	8.7 ± 0.2	…	3 ± 0.2
0.83	66.6	3×10^{16}	19.2 ± 0.2	17.6 ± 4	12.1 ± 0.1	11.9 ± 1.9	4.1 ± 0.3
		5×10^{16}	25.6 ± 0.1	22.6 ± 4.5	10.5 ± 0.3	11 ± 2	6.6 ± 0.4
		1×10^{17}	21.4 ± 0.2	22 ± 4.8	10.2 ± 0.1	10.8 ± 1.8	3.2 ± 0.4
		2×10^{17}	23.5 ± 0.1	23.5 ± 4.6	10 ± 0.1	11.7 ± 2	2.9 ± 0.2
		3×10^{17}	20.5 ± 0.1	…	9.4 ± 0.2	…	3.1 ± 0.2
0.77	68.2	2×10^{17}	17.9 ± 0.3	19 ± 4	10.7 ± 0.3	11 ± 1.9	3.6 ± 0.2
		3×10^{17}	22.9 ± 0.2	21 ± 4	11.7 ± 0.2	12.3 ± 2	4.7 ± 0.3

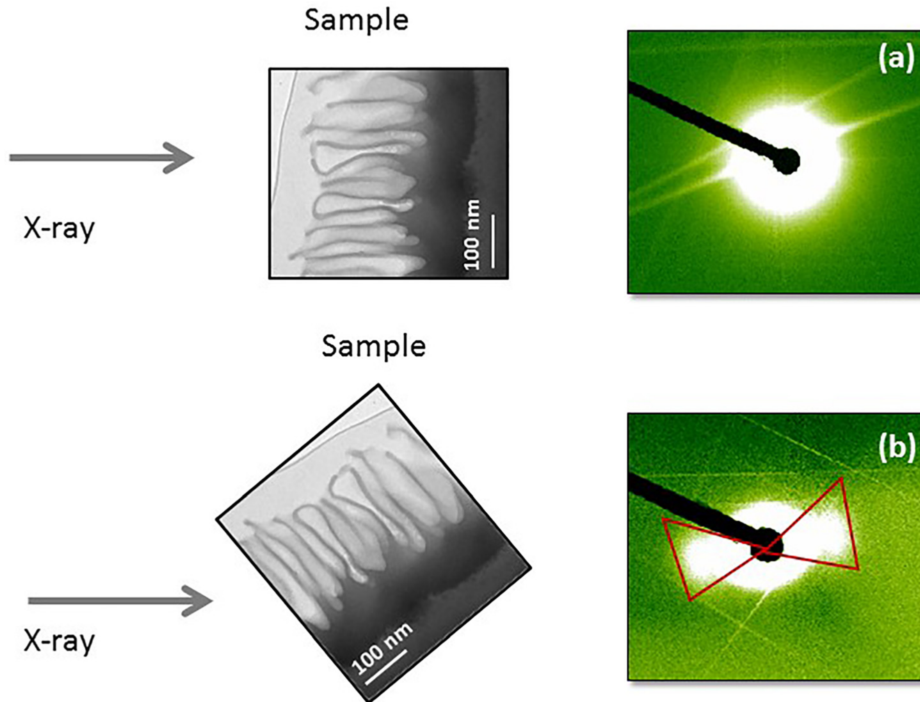

FIG. 1. SAXS measurement schematics and images for self-ion implantation of Ge with 140 keV at 2×10^{16} ions/cm^2 corresponding to porous structures (a) aligned with X-ray beam and (b) tilted by 45°.

the difference in electron density between the a-Ge sidewalls and the hollow pores. Thus, the obtained scattering curves contain detailed information on the porous layer.

In order to extract the scattering intensities from the short streaks or bulges, two masks on both sides of the bulges were applied (see Fig. 1(b)). The scattering intensities in these areas contain information about the pore morphologies. As apparent from the XTEM and SEM images in Fig. 3, the pores resemble long elongated, almost cylindrical hollow structures surrounded by solid, reasonably uniform sidewalls. For analysis of the SAXS data, we thus approximate the pores by cylinders with an empty core surrounded by a shell (the sidewalls) that is all aligned normal to the sample surface. The cylindrical core-shell model applied is shown in Fig. 2 with a hollow core radius R_c and sidewall (shell) thickness T_s. This model has also been previously used to fit ion track scattering in amorphous SiO_2.[29]

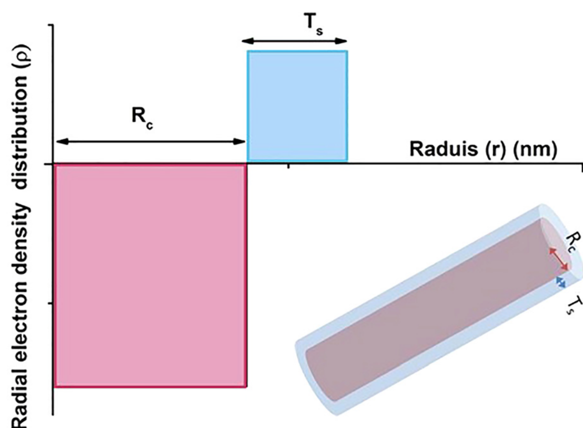

FIG. 2. Schematic radial density profile of the cylindrical core-shell model used to extract the pore radii and sidewall thicknesses of the pores from the SAXS images.

The form factor used for the cylindrical core-shell model is[29]

$$F(q) = \frac{2\pi L\rho_c}{q}\left[\left(1-\frac{\rho_s}{\rho_c}\right)R_c J_1(R_c q) + \frac{\rho_s}{\rho_c} R J_1(Rq)\right],$$

where L is the pore length, R_c the core radius, T_s is the shell thickness, and J_1 Bessel function of the first order. The total cylinder (pore) radius is $R = R_c + T_s$.

The polydisperse nature of the pores was taken into account in the form of a Gaussian radius distribution with standard deviation σ_r for the core radius, which is rescaled for the entire radius R. The scattering intensity I(q) for the cylindrical core-shell model can then be written as[29]

$$I(q_r) \propto \int \frac{1}{\sqrt{2\pi\sigma_r}} \exp\left\{-\frac{(r-R_C)^2}{2\sigma_r{}^2}\right\} |f(q_r, r)|^2 \, dr.$$

B. Nanopores in Ge as a function of ion fluence

Self-ion implantation of Ge forms porous structures at relatively moderate ion fluences $>10^{15}$ ions/cm^2 that develop further with ongoing implantation. Fig. 3 shows plain-view (PVSEM) (a)–(e) and cross-section (XTEM) (f)–(j) images for Ge irradiated at RT to ion fluences of 5×10^{15}, 1×10^{16}, 2×10^{16}, 5×10^{16}, and 1×10^{17} ions/cm^2, respectively. The pore size observed on the sample surface increases with increasing ion fluence as shown by the PVSEM images in Figs. 3(a)–3(e). The XTEM micrographs show columnar pores surrounded by sidewalls with an underlying amorphous layer. The pore radius ranges from 4 to 14 nm and saturated at fluence of 5×10^{16} ions/cm^2 as we have reported previously.[8] Clearly, the thickness of the porous layer also increased with increasing ion fluence as apparent from Figs. 3(f)–3(j). The thickness of the porous layer is increased from

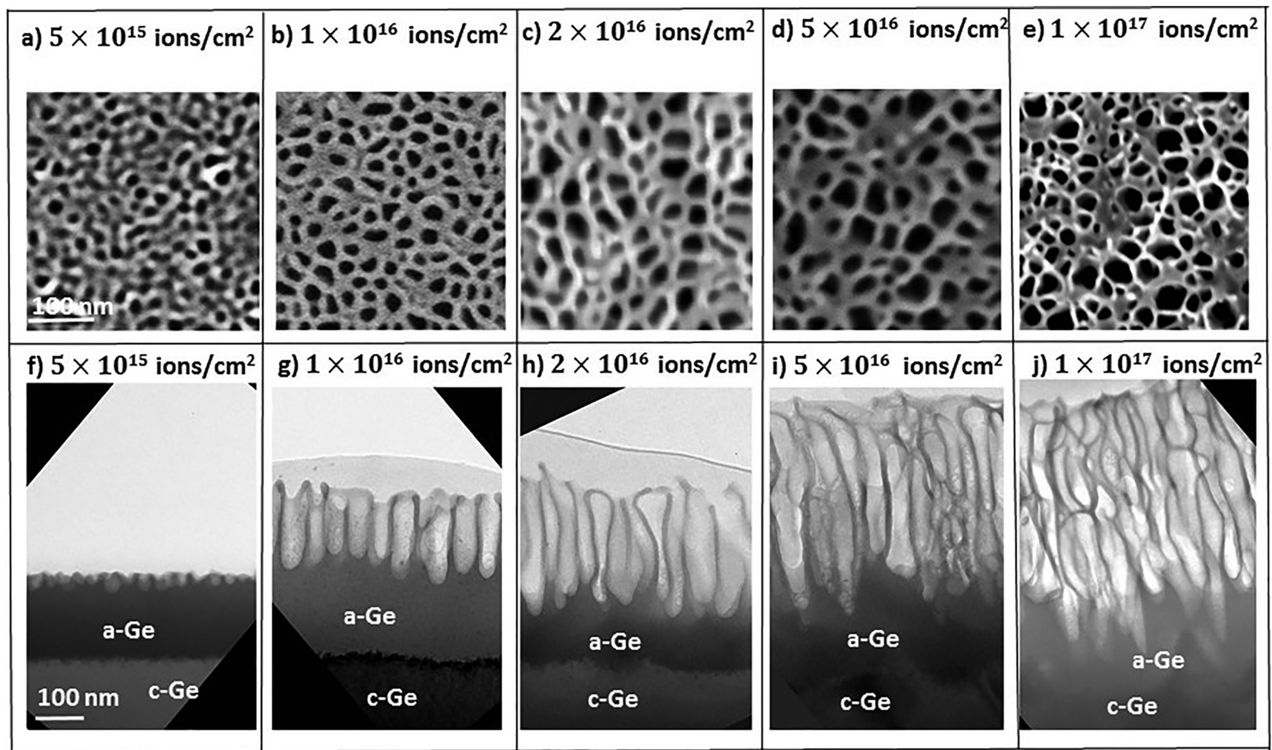

FIG. 3. PVSEM (upper row) and XTEM (lower row) images, for self-ion implantation of Ge implanted with 140 keV at room temperature at (a) and (f) 5×10^{15} ions/cm^2, (b) and (g) 1×10^{16} ions/cm^2, (c) and (h) 2×10^{16} ions/cm^2, (d) and (i) 5×10^{16} ions/cm^2, and (e) and (j) 1×10^{17} ions/cm^2. The scale bar is the same for all SEM and TEM images, respectively.

30 nm to 516 nm for fluences of 5×10^{15} and 1×10^{17} ions/cm^2, respectively. Pore formation developed with ongoing ion implantation, leading to a complex and overlapped porous structure which makes the pore size characterization by TEM non-trivial.[8] However, the pore width observed from TEM does not seem to change significantly while it appears to increase from SEM. This is most likely a surface effect, as it will also be shown in SAXS analysis later that the pore width does not increase significantly.

The difference in electron density between the a-Ge sidewall and the hollow pores results in anisotropic scattering for Ge samples implanted to ion fluences of 1×10^{16}, 2×10^{16}, and 5×10^{16} ions/cm^2, which are shown in Figs. 4(a)–4(c) and corresponds to the XTEM images in Figs. 3(g)–3(i), where porous layer thickness increased by 51%, 71%, and 72% for fluences of 1×10^{16}, 2×10^{16}, and 5×10^{16} ions/cm^2, respectively. We note that the narrow straight scattering lines observed in the scattering patterns in Fig. 4 result from inelastic scattering from the crystalline Ge substrate.

Fig. 5(a) shows the background subtracted scattering intensities for porous Ge as extracted from the bulges shown in the SAXS images of Fig. 4. It is clear from Fig. 5(a) that there are distinct oscillations for all scattering intensities, which are different than those from unimplanted Ge. The SAXS data were fitted to the model described in the previous section. All the results from SAXS and TEM are summarized in Table I, including pore radii and sidewall thicknesses. In Figs. 5(b) and 5(c), the pore radii and sidewall thicknesses extracted from SAXS, SEM and TEM are plotted as a function of the ion fluence. The results of TEM and SAXS are in remarkable agreement for both quantities, whereas SEM results differ in both pore radius and sidewall thickness. It is apparent from Fig. 5(b) that the core radius increases from 11.8 nm at an ion fluence of 5×10^{15} ions/cm^2, where the porous structure starts to nucleate, to 23.9 nm at an ion fluence of 1×10^{16} ions/cm^2 where the pore structure is well developed. With further implantation, the core radius fluctuates with a net decrease up to a fluence of 1×10^{17} ions/cm^2. At 2×10^{17} ions/cm^2, the value increases again, which might be due to the complex porous structure that is formed at high ion fluences as it shown in Figs. 3(e) and 3(j). The pore radius in SEM is far less compared to TEM and SAXS, and

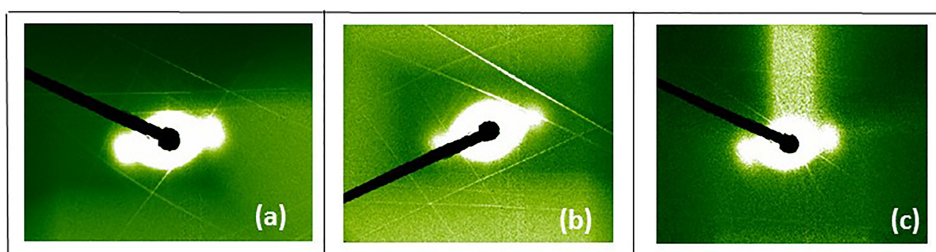

FIG. 4. X-ray scattering images under 45° tilt for Ge implanted with 140 keV at RT at fluences of (a) 1×10^{16} ions/cm^2, (b) 2×10^{16} ions/cm^2, and (c) 5×10^{16} ions/cm^2.

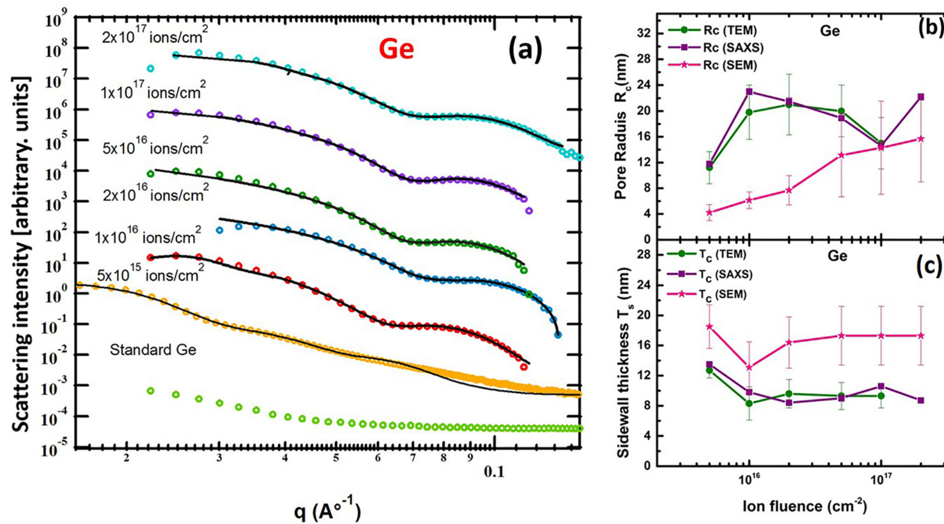

FIG. 5. (a) Scattering intensities from nano-porous structures in Ge for fluences of 5×10^{15}, 1×10^{16}, 2×10^{16}, 5×10^{16}, 1×10^{17}, and 2×10^{17} ions/cm^2 implanted with 140 keV Ge ions after background removal as a function of scattering vector q. The solid lines are the corresponding fits to the core-shell cylindrical model. (b) The pore radius as a function of fluence from TEM, SEM, and SAXS analyses. (c) The sidewall thickness of the pores as a function of fluence from TEM, SEM, and SAXS analyses.

that is likely to be a surface effect, where a wide distribution of pores is observed. Factors influencing this can be an increased surface sputtering rate, re-deposition of sputtered atoms at the surface, and the tendency to reduce the surface free energy.

The sidewall thickness, on the other hand, decreases from about 13.5 nm at the onset of pore formation, i.e., at an ion fluence of 5×10^{15} ions/cm^2, to $\sim$9.8 nm at an ion fluence of 1×10^{16} ions/cm^2 and remains constant for any further increase in ion fluence as shown in Fig. 5(c). This behavior is consistent with findings of Romano *et al*.[30] In contrast, SEM shows larger sidewall thickness compared to TEM and SAXS. This can again be attributed to a surface effect mediated by the processes mentioned above. In fact, it is apparent from the TEM images (see, for example, Figs. 3(g) and 3(h)) that near the surface the sidewalls have the tendency to "bend" inwards at the surface, which is consistent with the observation of smaller pores on larger sidewalls in the plan-view SEM images.

Figs. 6(a)–6(c) show the core radius distributions and Figs. 6(d)–6(f) the sidewall thickness distributions as obtained by SEM, TEM, and SAXS. Clearly, there is good agreement between TEM and SAXS for both core radius and shell thickness data. However, the sidewall thicknesses and pore radii obtained by SEM are significantly different. This is due to the fact that SEM only probes the sample surface; SAXS and TEM on the other hand take the entire pore into account. It is clear that TEM is very consistent with SAXS which both show only little ion fluence dependence beyond the onset of porosity at 5×10^{15} ions/cm^2. On the other hand, the pore radius observed by SEM exhibits a clear dependence on ion fluence with an increase in radius with increasing ion fluence from 5 to 8.5 for fluences between 5×10^{15} to 2×10^{16} ions/cm^2. About three decades ago, Wilson[9] has reported that pore diameter increases from 45 nm to 120 nm with increasing ion fluence and saturates at a high fluence of 10^{17} ions/cm^2 by using 60 keV Ge ions. He interpreted the reasons for this effect as a combination of factors involving sputtering, flux enhancement, radiation damage, swelling, and redisposition. Romano *et al*.[30] also found that pore radius increased with ion fluence by using SEM images.

In the case of the sidewall thicknesses (Figs. 6(d)–6(f)), SEM shows slightly larger thicknesses than TEM and SAXS. We again attribute this to surface effects.

C. Nanopores in $Si_{1-x}Ge_x$ alloys as a function of ion fluence

The onset of pore formation is shifted to a higher ion fluence of 8×10^{15} ions/cm^2 in $Si_{0.17}Ge_{0.83}$ and 1×10^{17} ions/cm^2 for $Si_{0.23}Ge_{0.77}$ compared to Ge as we previously reported.[8] XTEM images and scattering patterns of $Si_{0.17}Ge_{0.83}$ implanted to an ion fluence of 5×10^{16} and 1×10^{17} ions/cm^2 are shown in Figs. 6(a)–6(d). For $Si_{0.23}Ge_{0.77}$ alloy, the XTEM and SAXS scattering images for ion fluence of 2×10^{17} and 3×10^{17} ions/cm^2 are shown in Figs. 6(e)–6(h). The thicknesses of the porous layers increased from 95 to 130 nm for $Si_{0.17}Ge_{0.83}$ and from 55 to 72 nm for $Si_{0.23}Ge_{0.77}$, respectively. The SAXS patterns of $Si_{0.17}Ge_{0.83}$ show almost isotropic scattering that correlates to the small aspect ratio of the observed pores in the cross section images that are shown in Figs. 6(a) and 6(b). This trend is further enhanced in $Si_{0.23}Ge_{0.77}$ as the degree of porosity is further reduced in this composition. Indeed, when the porous layer thickness become less than 20% of the thickness of amorphous layer, there was a continuous modification in the shape of the scattering profiles.[31]

Fig. 10 shows the effect of Ge content on the feature size of the nano-pores. It is apparent that for samples implanted at room temperature, decreasing the Ge fraction from 100 to 77 at. % leads to an increase in the sidewall thickness of about 20% at an ion fluence of 2×10^{17} ions/cm^2.

It is clear from our previous study that the pores nucleate usually at the surface in pure Ge for all studied conditions (at different ion fluences and irradiation temperatures). Although sputter erosion occurs, swelling is always dominant in Ge due to the initiation of porosity at moderate ion fluences of 5×10^{15} ions/cm^2 where the sputtering rate is small. Wilson[9] reported that the sputter etching may play an important role in pore formation. The mechanism of porosity is based on point defect (vacancies and interstitials) movement and mobility in pure Ge near the surface, leading to

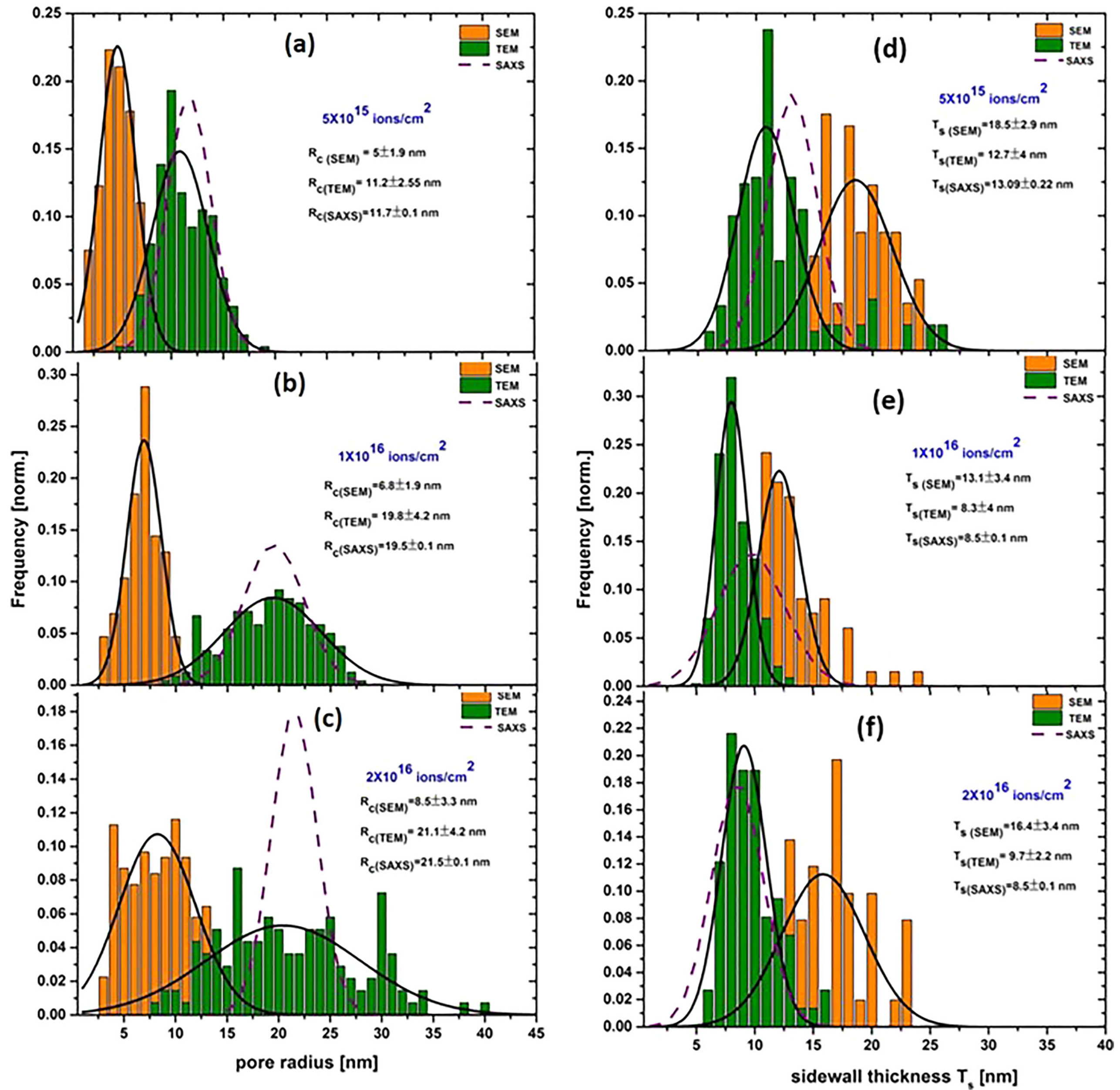

FIG. 6. Distribution for the pore radii (left) and sidewall thicknesses (right) obtained from SEM, TEM, and SAXS for self-ion implantation of Ge irradiated with (a) and (d) 5×10^{15} ions/cm^2, (b) and (e) 1×10^{16} ions/cm^2, and (c) and (f) 2×10^{16} ions/cm^2. The solid lines show the Gaussian fits to the SEM and TEM data.

vacancy clustering followed by the formation of small voids at the early stages at 5×10^{15} ions/cm^2, as shown in Fig. 3(f). This process occurs after the amorphization process because void formation is not favoured in crystalline Ge as vacancy agglomeration is not sufficient. Additionally, the difference in diffusion properties between vacancies and interstitials plays an important role in the formation of porosity. For instance, if the vacancies move faster than interstitials, vacancies are more likely cluster and grow as shown in Figs. 3(b) and 3(g), while interstitials migrate between the voids to increase the height of the sidewalls and recombine at some stage.[32] The sidewall thickness ultimately saturates and remains constant with increasing ion fluence as shown from TEM and SAXS data. This happens when the sidewall thickness reaches some typical vacancy diffusion length. This was also observed in nanofiberous networks in GaSb[6] where the fiber thickness does not change because the inter-void distances are sufficiently small for vacancies to diffuse to the walls where they annihilate at the void surface, instead of forming new voids.

D. Nanopores in $Si_{1-x}Ge_x$ alloys as a function of ion fluence

The onset of pore formation is shifted to a higher ion fluence of 8×10^{15} ions/cm^2 in $Si_{0.17}Ge_{0.83}$ and 1×10^{17} ions/cm^2 for $Si_{0.23}Ge_{0.77}$ compared to Ge as we previously reported.[8] XTEM images and scattering patterns of $Si_{0.17}Ge_{0.83}$ implanted to an ion fluence of 5×10^{16} and 1×10^{17} ions/cm^2 are shown

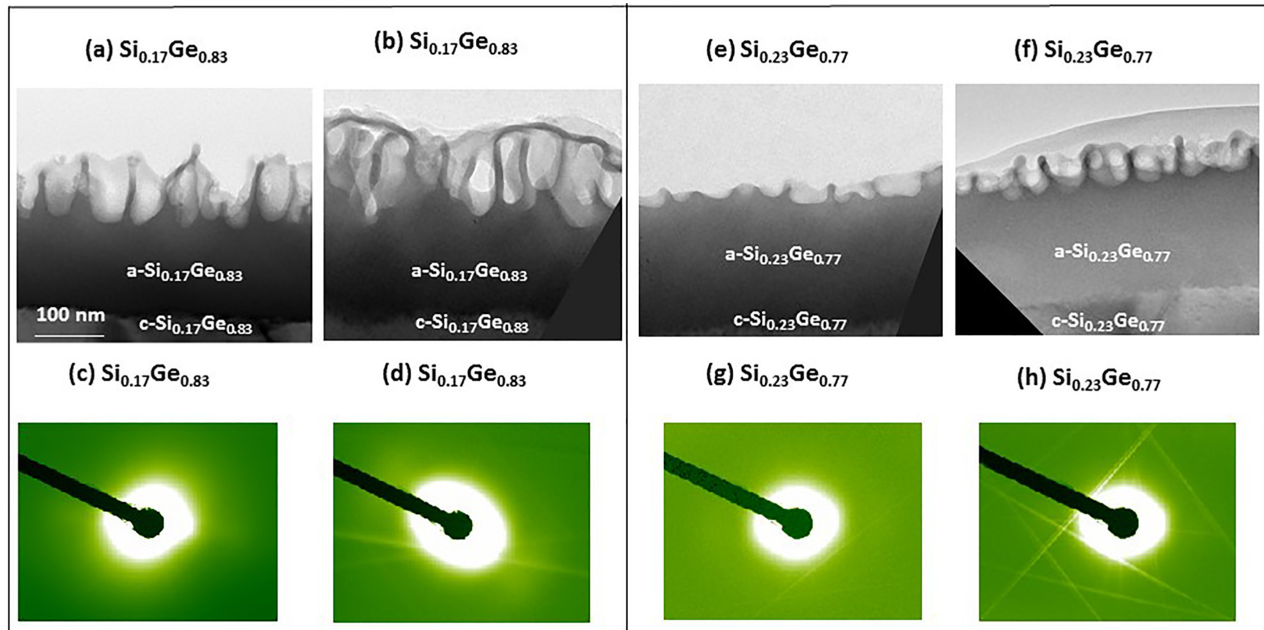

FIG. 7. XTEM images and X-ray scattering images under 45° tilt for $Si_{0.17}G_{0.83}$ and $Si_{0.17}Ge_{0.77}$ implanted at RT: (a) and (c) 5×10^{16} ions/cm^2 of $Si_{0.17}G_{0.83}$, (b) and (d) 1×10^{17} ions/cm^2 of $Si_{0.17}G_{0.83}$, (e) and (g) 2×10^{17} ions/cm^2 of $Si_{0.23}G_{0.77}$, and (f) and (h) 3×10^{17} ions/cm^2 of $Si_{0.23}G_{0.77}$. The scale bar is the same for all images.

in Figs. 7(a)–7(d). For $Si_{0.23}Ge_{0.77}$, the XTEM and SAXS scattering images for ion fluences of 2×10^{17} and 3×10^{17} ions/cm^2 are shown in Figs. 7(e)–7(h). The thicknesses of the porous layers increased from 95 to 130 nm for $Si_{0.17}Ge_{0.83}$ and from 55 to 72 nm for $Si_{0.23}Ge_{0.77}$, respectively. The SAXS patterns of $Si_{0.17}Ge_{0.83}$ show almost isotropic scattering that correlates to the small aspect ratio of the observed pores in the cross section images that are shown in Figs. 7(a) and 7(b). This trend is further enhanced in $Si_{0.23}Ge_{0.77}$ as the degree of porosity is further reduced in this composition. Indeed, when the aspect ratio of porous layer decreases, the scattering pattern becomes more isotropic as expected.

In the case of the alloys, much less pronounced oscillations are apparent in the scattering intensities for all investigated ion fluences as shown in Figs. 8(a) and 9(a). The pore radii and sidewall thicknesses shown in Figs. 8, 9(b), and 9(c) show good agreement between SAXS and TEM results. Similar to the case for Ge, the pore radius increases in the early stage, then is somewhat independent on ion fluence and tends to fluctuate with further irradiation. The sidewall initially decreases and then remains approximately constant.

In $Si_{0.17}Ge_{0.83}$ the pore radius displayed in Fig. 8(b) at the earlier stage of porous structure development at 3×10^{16} ions/cm^2 is 19.2 nm. With increasing ion fluence of 5×10^{16} ions/cm^2, the radius is slightly increased at 25.6 nm where the porous structure is developed and fluctuates with further irradiation. However, the sidewall thickness is slightly higher at lower fluence of 3×10^{16} ions/cm^2 at 12.1 nm (see Fig. 8(c)). When the porous structure is developed at 5×10^{16} ions/cm^2, the sidewall drops off to 10.5 nm and becomes

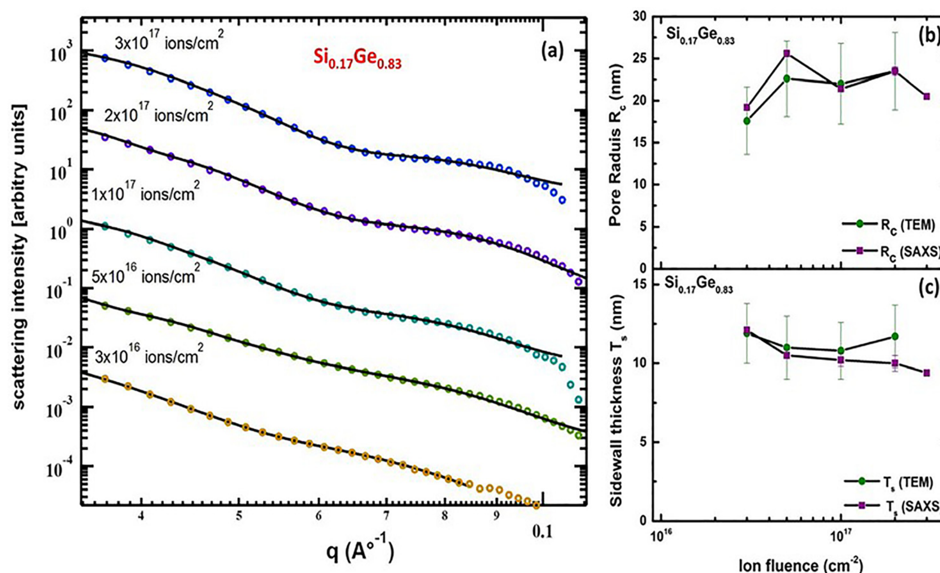

FIG. 8. (a) Scattering intensities from nano-porous structures in $Si_{0.17}Ge_{0.83}$ for fluences of 3×10^{16}, 5×10^{16}, 1×10^{17}, 2×10^{17}, and 3×10^{17} ions/cm^2 implanted with 140 keV Ge ions after background removal as a function of scattering vector q. The solid lines are the corresponding fits with the core-shell cylindrical model. (b) The pore radius as a function of fluence from both TEM and SAXS analyses. (c) The sidewall thickness as a function of fluence from both TEM and SAXS analyses.

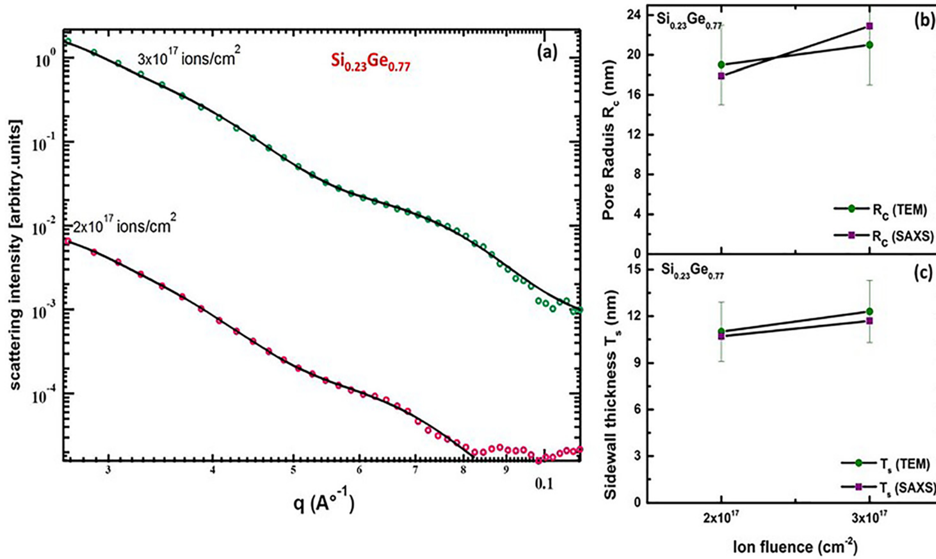

FIG. 9. (a) Scattering intensities from nano-porous structures in $Si_{0.23}Ge_{0.77}$ for fluences of 2×10^{17} and 3×10^{17} ions/cm^2 implanted with 140 keV Ge ions after background removal as a function of scattering vector q. The solid lines are the corresponding fits with the core-shell cylindrical model. (b) The pore radius as a function of fluence from both TEM and SAXS analyses. (c) The sidewall thickness as a function of fluence from both TEM and SAXS analysis.

stable under further implantation. The sidewall thickness in $Si_{0.17}Ge_{0.83}$ is similar to Ge. There are only 2 data points for $Si_{0.23}Ge_{0.77}$ for the sidewall thickness indicating an increase with increasing fluence. The width of the Gaussian distribution (polydispersity) of the core radii and sidewall thicknesses is in the order of 10% when the porous structure is developed.

In the case of $Si_{0.23}Ge_{0.77}$, the pore radius ranged from 17.9 and 22.9 for 2×10^{17} ions/cm^2 and 3×10^{17} ions/cm^2, respectively. We note that the early stages of pore formation for this alloy require a fluence of 2×10^{17} ions/cm^2 as it can be seen from Figs. 7(e) and 7(f). At 3×10^{17} ions/cm^2, the porous structure is still developing slowly. However, the sidewall was found to be increasing slightly from 10.7 to 11.7 nm. The width of the Gaussian distribution (polydispersity) ranged between 30% and 40% of the sidewall thickness. Increasing the Ge content leads to a slight reduction in the sidewall thickness.

Fig. 10 shows the effect of Ge content on the feature size of the nano-pores. It is apparent that for samples implanted at room temperature, decreasing the Ge fraction from 100 to 77 at. % leads to an increase in the sidewall thickness of about 20% at an ion fluence of 2×10^{17} ions/cm^2.

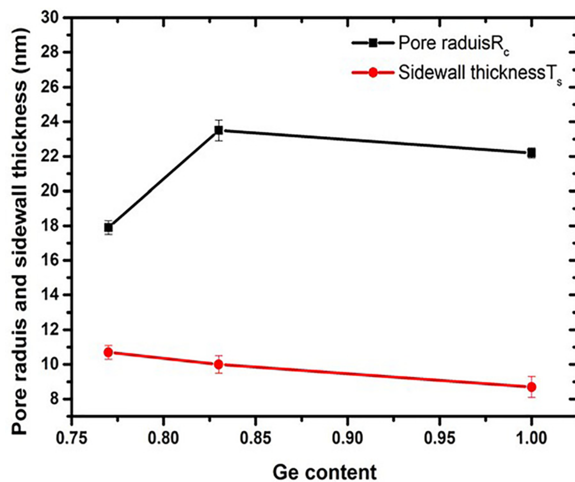

FIG. 10. Pore radii and sidewalls thicknesses as a function of Ge content for samples implanted at RT at a fluence of 2×10^{17} ions/cm^2.

In our previous study,[8] we found that the initiation of porosity in SiGe alloys is also started at the surface after forming an amorphous phase and is pushed to higher fluences. This may be because of a decrease in the vacancy mobility that results in a loss of vacancies to recombination, which then leads to small porous layer thickness compared to Ge. In fact, previous literature suggests that vacancy clustering does not occur readily in Si below 300 °C. Therefore, the presence of Si atoms in the matrix leads to lower the vacancy mobility and hence decreases vacancy clustering.

We speculate that the dominant mechanisms for pore formation in SiGe alloys are preferential sputtering and non-uniform surface elemental segregation of Si and Ge. The latter can be inferred from increased roughness observed in step height measurements. Indeed, it becomes difficult to initiate porosity when Si is present in the matrix as a result of the lower vacancy mobility in Si, indicated by the lower thickness of the porous layers in SiGe alloys in Figs. 7(a), 7(b), 7(e), and 7(f), compared to Ge. The different size of pores and sidewall thicknesses in the alloy compared to Ge maybe due to the different mobility of point defects. After preferential sputtering and elemental segregation, if the vacancy mobility increases, they travel faster to pore interfaces where they recombine and the sidewall thickness will increase. At the high ion fluence, we expect the sidewalls are in saturation. However, more experiments are required to confirm that these mechanisms are operational.

In $Si_{0.23}Ge_{0.77}$, it is very difficult to form a porous structure as the Si content is further increased and sputtering is dominant. This requires an even higher ion fluence of 2×10^{17} ions/cm^2 to lead to the early stage of pore formation, and thus, it will show a slightly larger sidewall thickness and hence a smaller pore radius as is demonstrated in Fig. 6(e).

E. Nano-pore formation in Ge/$Si_{1-x}Ge_x$ alloys as function of implantation temperature

The aim of this section is to study the effect of the implantation temperature on the nano-porous structure sizes. In our previous work,[8] we observed the formation of porous

TABLE II. SAXS and TEM results of pore radii and sidewall thicknesses at different implantation temperatures for Ge and $Si_{0.17}Ge_{0.83}$.

Ge content	Ion fluence (cm^{-2})	Implantation temperature (°C)	Core radius R_c (nm) SAXS	Core radius R_c (nm) TEM	Shell thickness T_s (nm) SAXS	Shell thickness T_s (nm) TEM	Polydispersity (nm) SAXS
1	1×10^{16}	70	27.4 ± 0.3	24 ± 9.8	10.7 ± 0.2	9 ± 1.7	4.3 ± 0.7
		150	28.5 ± 0.6	26 ± 6.9	11.5 ± 0.2	10.4 ± 2	5.2 ± 0.9
		200	31.7 ± 0.4	…	12 ± 0.2	…	4.9 ± 0.8
0.83	1×10^{17}	50	27 ± 0.5	25.3 ± 15.2	10.1 ± 0.2	11.3 ± 3.1	2.6 ± 0.2
		70	30.8 ± 0.6	…	10.7 ± 0.2	…	5.9 ± 0.2
		200	33.5 ± 0.3	28.3 ± 15.2	12.9 ± 0.2	12.8 ± 3.9	3.3 ± 0.4

structures at implantation temperatures between −80 and 240 °C for Ge and between −60 and 300 °C for the $Si_{0.17}Ge_{0.83}$ alloy. The pores appeared to slightly increase in size with increasing implantation temperature as observed by PVSEM. However, XTEM micrographs show that the thickness of the porous layer decreased with increasing temperature and the underlying amorphous layer thickness also decreased at elevated temperatures due to dynamic annealing (for more details, see Ref. 8). The SAXS and TEM measurements performed here show an increase in both pore radii and sidewall thickness with increasing temperature. The results from SAXS and TEM are summarised in Table II and shown in Fig. 11.

Fig. 11 shows SAXS scattering intensities and the pore radius and sidewall thickness for Ge implanted with 1×10^{16} ions/cm^2 at 70, 150, and 200 °C, and $Si_{0.17}Ge_{0.83}$ implanted with 1×10^{17} ions/cm^2 at 50, 70, and 200 °C ((c) and (d)). Clearly, there are distinct oscillations observed corresponding to nanoporous structures.

It is apparent the oscillations shift to lower q with increasing temperature for both Ge and $Si_{0.17}Ge_{0.83}$. This indicates the pore radius and sidewall thicknesses are increasing as a result of the temperature. The mean pore radius and sidewall thickness is in a good agreement between SAXS and TEM as plotted in Figs. 11(b) and 11(d) for Ge and $Si_{0.17}Ge_{0.83}$, respectively. The pore radius increases with

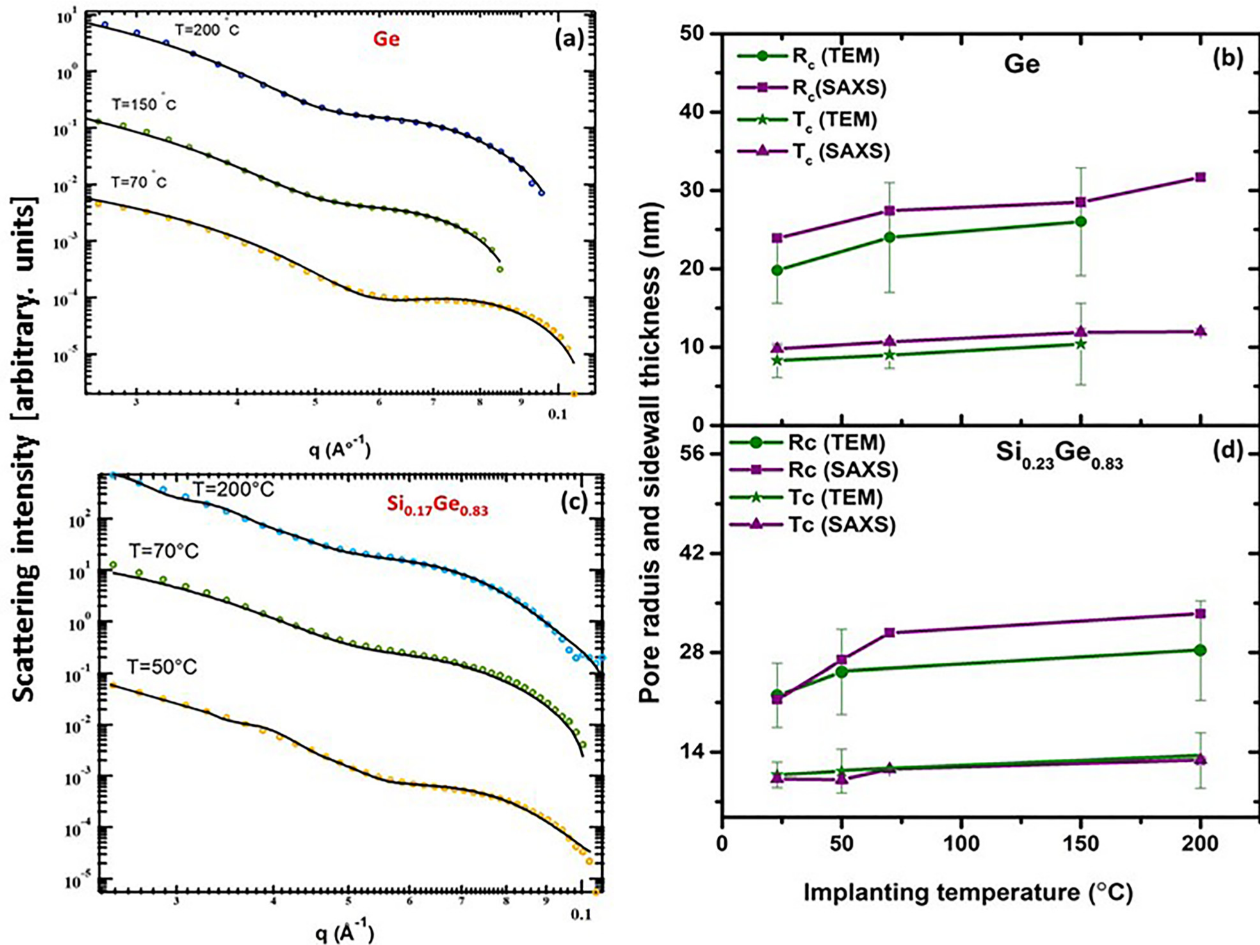

FIG. 11. Scattering intensities from porous structures in (a) Ge, and (c) $Si_{0.17}Ge_{0.83}$, implanted with 140 keV Ge ions at elevated temperatures after background removal as a function of scattering vector q. The solid lines are the corresponding fits to the core-shell cylindrical model. (b) Pore radius and sidewall thickness in Ge as a function of implanting temperature. (d) pore radius and sidewall thickness in $Si_{0.17}Ge_{0.83}$ as a function of implanting temperature.

increasing temperature from 23.5 at RT to 31 nm at 200 °C, and the sidewall thickness increases slightly by ∼2 nm from 9.8 to 12 nm between implantation at RT and 200 °C for Ge. In $Si_{0.17}Ge_{0.83}$, a similar trend is observed with an increase in the pore mean radius from 21.4 to 33 nm and in the sidewall thickness from 10.2 to 12.9 nm between RT and 200 °C.

We can conclude that both porous radii and sidewall thicknesses are increased with increasing temperature. The increasing of pore radii was already demonstrated by PVSEM images in the previous study,[8] and the amorphous layer decreases in thickness due to thermal annealing. It is possible to explain the temperature dependent behavior in terms of the diffusivity of both vacancies and interstitials, which increases with increasing temperature, and thus, we expect larger sidewalls and pore radii. This is consistent with previous investigations in GaSb as it showed that the nanofiber size depended on implant temperature.[6] When the vacancies are more mobile, they contribute to the pores by recombining at the pore surface. At increased implant temperatures, the increased vacancy mobility leads to an increased typical diffusion length, which in turn leads to an increased sidewall thickness.

IV. CONCLUSIONS

Complementary SAXS and XTEM were used to characterize ion irradiation induced porosity in Ge, $Si_{0.17}Ge_{0.83}$, and $Si_{0.23}Ge_{0.77}$ alloys as a function of ion fluence and irradiation temperature and compared with PVSEM measurements. SAXS and TEM yield pore radii and sidewall thicknesses with regard to entire bulk, whereas PVSEM provides information about the porous layer surface. We demonstrated that a cylindrical core-shell structure with a hollow core provides an appropriate model to fit the SAXS data and is in excellent agreement with results from TEM. We found the important following characteristics: (i) the pore radii do not increase markedly after the development of porous structure in both Ge and SiGe alloys. (ii) The sidewall thickness increases slightly with increasing Si content. (iii) Both the sidewall thickness and pore radii increase at elevated temperature due to higher diffusivity of point defects.

ACKNOWLEDGMENTS

We acknowledge access to NCRIS facilities (ANFF and the Heavy Ion Accelerator Capability) and the Center for Advanced Microscopy, both at the Australian National University. P.K. and M.C.R. thank the Australian Research Council, and Imam Abdulrahman Bin Faisal University for financial support. This research was undertaken on the SAXS/WAXS beamline at the Australian Synchrotron.

[1] G. Q. Lu and X. S. Zhao, in *Nanoporous Materials Science and Engineering*, edited by G. Q. Lu and X. S. Zhao (Imperial College Press, London, 2004).
[2] B. S. Don, J. Korean Phys. Soc. **56**(1), 113 (2010).
[3] D. A. Lavan, T. McGuire, and R. Langer, Nat. Biotechnol. **21**(10), 1184–1191 (2003).
[4] B. Kang and G. Ceder, Nature **458**(7235), 190–193 (2009).
[5] L. Bischoff, W. Pilz, and B. Schmidt, J. Appl. Phys. **104**(4), 1153–1158 (2011).
[6] S. M. Kluth, J. D. F. Gerald, and M. C. Ridgway, Appl. Phys. Lett. **86**(13), 131920 (2005).
[7] S. M. Kluth, D. Llewellyn, and M. C. Ridgway, Nucl. Instrum. Methods Phys. Res., Sect. B **242**(1–2), 640–642 (2006).
[8] H. S. Alkhaldi, F. Kremer, T. Bierschenk, J. L. Hansen, A. Nylandsted-Larsen, J. S. Williams, and M. C. Ridgway, J. Appl. Phys. **119**(9), 094303 (2016).
[9] I. H. Wilson, J. Appl. Phys. **53**(3), 1698 (1982).
[10] B. R. Appleton, O. W. Holland, J. Narayan, O. E. Schow, J. S. Williams, K. T. Short, and E. Lawson, Appl. Phys. Lett. **41**(8), 711–712 (1982).
[11] O. Holland, B. Appleton, and J. Narayan, J. Appl. Phys. **54**(5), 2295–2301 (1983).
[12] G. Impellizzeri, L. Romano, L. Bosco, C. Spinella, and M. G. Grimaldi, Appl. Phys. Express **5**(3), 035201 (2012).
[13] H. Gleiter, Acta Mater. **48**(1), 1–29 (2000).
[14] S. S. Chang and R. E. Hummel, J. Lumin. **86**(1), 33–38 (2000).
[15] J.-S. Yu, S. Kang, S. B. Yoon, and G. Chai, J. Am. Chem. Soc. **124**(32), 9382–9383 (2002).
[16] M. E. Davis, Nature **417**(6891), 813–821 (2002).
[17] P. Fratzl, G. Vogl, and S. Klaumünzer, J. Appl. Crystallogr. **24**(5), 588–592 (1991).
[18] P. Goudeau, A. Naudon, A. Halimaoui, and G. Bomchil, J. Lumin. **57**(1), 141–145 (1993).
[19] K. Omote, Y. Ito, and S. Kawamura, Appl. Phys. Lett. **82**(4), 544–546 (2003).
[20] P. Goudeau, A. Naudon, V. Vezin, A. Halimaoui, G. Bomchil, and B. Lambert, Phys. Status Solidi B **190**(1), 63–68 (1995).
[21] K. Suresh, M. Ohnuma, Y. Oba, N. Kishimoto, P. Das, and T. Chini, J. Appl. Phys. **107**(7), 073504 (2010).
[22] S. Mazumder, D. Sen, and A. Patra, Pramana **63**(1), 165–173 (2004).
[23] D. Sen, S. Mazumder, and S. Tarafdar, J. Mater. Sci. Lett. **37**(5), 941–947 (2002).
[24] M. Engel, B. Stühn, J. J. Schneider, T. Cornelius, and M. Naumann, Appl. Phys. A **97**(1), 99–108 (2009).
[25] V. Vezin, P. Goudeau, A. Naudon, A. Halimaoui, and G. Bomchil, Appl. Phys. Lett. **60**(21), 2625–2627 (1992).
[26] M. Binder, T. Edelmann, T. H. Metzger, G. Mauckner, G. Goerigk, and J. Peisl, Thin Solid Films **276**(1–2), 65–68 (1996).
[27] J. F. Ziegler, J. P. Biersack, and U. Littmark, *The Stopping and Range of Ions in Solids* (Pergamon, New York, 1984).
[28] D. B. Williams and C. B. Carter, *The Transmission Electron Microscope* (Springer, 1996).
[29] P. Kluth, C. Schnohr, O. Pakarinen, F. Djurabekova, D. Sprouster, R. Giulian, M. C. Ridgway, A. Byrne, C. Trautmann, and D. Cookson, Phys. Rev. Lett. **101**(17), 175503 (2008).
[30] L. Romano, G. Impellizzeri, M. V. Tomasello, F. Giannazzo, C. Spinella, and M. G. Grimaldi, J. Appl. Phys. **107**(8), 084314 (2010).
[31] A. Naudon, P. Goudeau, A. Halimaoui, and G. Bomchil, J. Phys. IV **3**(C8), C8-349–C348-352 (1993).
[32] N. Nitta, M. Taniwaki, Y. Hayashi, and T. Yoshiie, J. Appl. Phys. **92**(4), 1799 (2002).